Chemical Science

EDGE ARTICLE

View Article Online
View Journal | View Issue

Cite this: *Chem. Sci.*, 2019, **10**, 3602

All publication charges for this article have been paid for by the Royal Society of Chemistry

Engineering high reversibility and fast kinetics of Bi nanoflakes by surface modulation for ultrastable nickel–bismuth batteries†

Yinxiang Zeng,[a] Mengying Wang,[a] Wanyi He,[a] Pingping Fang,[a] Mingmei Wu,*[a] Yexiang Tong,[a] Minghua Chen*[b] and Xihong Lu*[ab]

Received 7th November 2018
Accepted 11th February 2019

DOI: 10.1039/c8sc04967j

rsc.li/chemical-science

The exploration of a stable and high-rate anode is of pivotal importance for achieving advanced aqueous rechargeable batteries. Owing to the beneficial properties of high conductivity, suitable negative working voltage, and three-electron redox, bismuth (Bi) is considered as a promising anode material, but it suffers from poor stability. Here, we successfully endow Bi nanoflakes (NFs) with prominent cycling performance by a one-step surface oxidation approach to remarkably boost its reversibility. As a result, the partially oxidized Bi NFs (BiO_x) show an admirable capacity (0.38 mA h cm^{-2} at 2 mA cm^{-2}), good rate capability and superior long-term stability (almost no capacity decay after 20 000 cycles). Furthermore, a durable aqueous Ni//Bi battery is constructed based on the optimized BiO_x anode, which exhibits excellent durability with 96% capacity retention after 5000 cycles. This study could open a new avenue for the rational design of efficient anodes for eco-friendly and reliable aqueous rechargeable batteries.

Introduction

Economical, environmentally friendly, and reliable energy storage devices are critical for the widespread utilization of renewable-but-intermittent energy sources.[1–5] Among numerous candidates, aqueous rechargeable batteries (ARBs) have sparked extensive scientific interest owing to their intrinsically good safety, high ionic conductivities (~1 S cm^{-1}) and cost effectiveness.[6–9] In particular, aqueous rechargeable Ni//Zn batteries, which feature a high output voltage (~1.8 V), good rate capability, and materials that are abundant and eco-friendly, represent a compelling class of new energy storage devices.[10–13] For instance, Dai and his coworkers reported an ultrafast rechargeable Ni//Zn battery based on a deposited Zn anode, which delivered a high capacity of 0.307 mA h cm^{-2} and retained about 90% of its initial capacity after 600 cycles.[11] Additionally, an aqueous yarn-shaped NiCo//Zn battery using a Zn nanoflake (NF) anode achieved a high areal capacity of ~0.17 mA h cm^{-2} at 5 mA cm^{-2}, together with decent durability (60% capacity retention after 1000 cycles).[14] Despite this notable progress, the lifespan of most reported rechargeable Ni//Zn batteries is insufficient due to the irreversible reaction and dendrite formation on the Zn anode, diminishing the commercial competitive advantages of Ni//Zn batteries.[12,15] Hence, exploiting a new reliable and alternative anode with high reversibility as well as excellent stability is extremely desirable for long-life ARBs, yet it remains a formidable challenge.

Bismuth-based materials have shown great promise as desirable anodes for ARBs owing to their environmental friendliness, favorable negative working window in aqueous electrolyte, and fast 3-electron redox reactions.[16–18] To date, a variety of nanostructured bismuth-based materials including bismuth (Bi),[16,19] Bi_2O_3,[6,17] Bi_2O_3/graphene,[18] $(BiO)_4CO_3(OH)_2$,[20] *etc.* have been explored and showed impressive performance. Among them, Bi with its inherently metallic characteristic and low molecular weight presents particular advantages, favoring higher conductivity and theoretical capacity (384.8 mA h g^{-1}).[16,19] The Bi film was investigated to afford a capacity of 0.055 mA h cm^{-2} and 40% capacity attenuation after 90 cycles.[19] Based on a Bi hierarchical nanostructured anode, a $NiCo_2O_4$//Bi battery was firstly reported to exhibit a maximum energy density of 1.52 mW h cm^{-3} and 89% capacity retention over 1000 cycles.[16] Although significant achievement has been obtained, the major obstacles for actual application of Bi electrodes are their unsatisfactory cycling durability and capacity, particularly at high mass loading (>3.0 mg cm^{-2}).

To tackle these issues, herein we demonstrate an efficient and general surface oxidation strategy to effectively boost the

[a]MOE of the Key Laboratory of Bioinorganic and Synthetic Chemistry, The Key Lab of Low-carbon Chem & Energy Conservation of Guangdong Province, School of Chemistry, Sun Yat-Sen University, Guangzhou 510275, China. E-mail: luxh6@mail.sysu.edu.cn; ceswmm@mail.sysu.edu.cn

[b]Key Laboratory of Engineering Dielectric and Applications (Ministry of Education), Harbin University of Science and Technology, Harbin 150080, China. E-mail: mhchen@hrbust.edu.cn

† Electronic supplementary information (ESI) available. See DOI: 10.1039/c8sc04967j

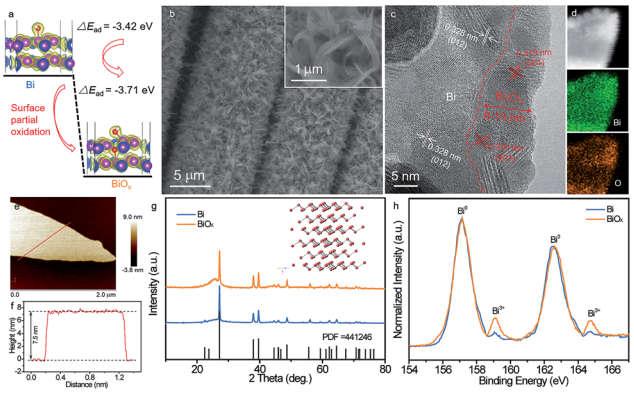

Fig. 1 (a) The calculated adsorption free energy changes of OH^- on the pristine Bi and BiO_x with the introduction of oxygen atoms. (b) SEM image, (c) TEM image (the red ring region presents the Bi_2O_3), and (d) EDS mapping of the BiO_x NFs. (e) AFM image of the BiO_x NFs and (f) the corresponding height profiles measured for the line in (e). (g) XRD patterns and (h) Bi 4f XPS spectra of the Bi and BiO_x NFs.

stability and capacity of Bi NFs by enhancing the electrochemical reaction reversibility. The Bi electrode will occur a redox reaction in alkaline media ($2Bi^0 + 6OH^- - 6e^- \rightleftharpoons Bi_2O_3 + 3H_2O$).[16] It is speculated that the adsorption properties of OH^- ions on the Bi surface have a vital effect on its redox reaction since OH^- takes part in the redox reaction.[21] To discover OH^- ion absorption on the surface of the electrode, density functional theory (DFT) calculation is applied as a guide before the experiments. As shown in Fig. 1a, the absorption energy of OH^- ions for Bi with the introduction of oxygen atoms on its surface (−3.71 eV) is much lower than that of pristine Bi (−3.42 eV), indicating that Bi with the introduction of oxygen atoms has a much stronger and easier capability for adsorbing OH^- ions. It is anticipated that the surface oxidation of Bi could enhance its absorption capability for OH^- ions, thus improving the electrochemical performance of the Bi electrode. Electrochemical results reveal that the partially oxidized Bi NFs (denoted as BiO_x) prepared by a facile controllable oxidation technique show unprecedented long-term cycling performance with negligible capacity decay even after 20 000 cycles, remarkably superior to the pristine Bi NFs (42.6% capacity retention). Moreover, by virtue of rich active sites and a fast electron/ion transport ability, the BiO_x NF electrode also has a high areal capacity (0.38 mA h cm^{-2} at 2 mA cm^{-2}) and an extraordinary rate capability. Additionally, based on this BiO_x anode, a robust and stable aqueous Ni//Bi battery is demonstrated, achieving a high energy density of 3.66 mW h cm^{-3} and outstanding cyclability (4% capacity attenuation after 5000 cycles), outperforming most currently reported ARBs.

Results and discussion

The partially oxidized Bi NFs were synthesized by a two-step process (Experimental section, ESI†). Firstly, the Bi NFs on carbon cloth were prepared by a facile electrodeposition approach with a potential of −0.8 V for 20 min (details in the Experimental section). Scanning electron microscopy (SEM) images (Fig. S1†) reveal that the surface of each carbon fiber is covered uniformly with Bi NFs without any binder, ensuring a favorable pathway for electron transfer and ion diffusion. After surface oxidation by a controllable successive water oxidation method (Experimental section), no obvious morphological change can be noticed for the BiO_x NFs (Fig. 1b). Further, structural features were investigated *via* the transmission electron microscopy (TEM) analysis of the BiO_x NFs (Fig. 1c), in which a lattice fringe with a *d*-spacing of 0.328 nm can be indexed to the (012) planes of metal Bi (JCPDS (Joint Committee on Powder Diffraction Standards) #44-1246). Another interplanar spacing of 0.319 nm matches well with the d_{201} spacing of Bi_2O_3 (JCPDS #65-1209), implying the coexistence of metallic Bi and Bi_2O_3 in the hybrid BiO_x NF sample. And the thickness of Bi_2O_3 is about 8–13 nm. In contrast, only lattice fringe spacings of 0.328 and 0.395 nm corresponding to Bi (JCPDS #44-1246) can be detected for the pristine Bi sample (Fig. S2†). The corresponding energy-dispersive spectroscopy (EDS) mapping images of the BiO_x NF sample clearly verify the homogeneous spatial distribution of Bi and O elements (Fig. 1d). Moreover, the atomic force microscopy (AFM) image in Fig. 1e and the corresponding height profile (Fig. 1f) of the BiO_x sample depict a single NF with an average thickness of ~7.5 nm.

The component of the pristine Bi and BiO_x samples was characterized by XRD and Raman analysis. As shown in Fig. 1g, except for the peak from carbon cloth, all the diffraction peaks for both samples fit well with the characteristic peaks of hexagonal Bi (JCPDS #44-1246), indicating the high purity of metallic Bi. Furthermore, Raman spectra illustrate that the two peaks located at 68.4 and 94.3 cm^{-1} for both samples can be assigned to the E_g and A_{1g} fundamental modes of metallic Bi, respectively (Fig. S3†).[16,22] There are no other signals of Bi_2O_3 or other bismuth oxides detected for the BiO_x sample in XRD or Raman spectra, which may be ascribed to the low content of oxygen. To further investigate the surface oxidation state of the pristine Bi and BiO_x samples, X-ray photoelectron spectroscopy (XPS) measurement was conducted. Fig. 1h compares the core level Bi 4f XPS spectra of the pristine Bi and BiO_x samples, where the peaks centered at 157.1 and 162.5 eV can be indexed to the typical $4f_{7/2}$ and $4f_{5/2}$ peaks of Bi^0, respectively, and the peaks at 159.1 and 164.7 eV correspond to the characteristic peaks of Bi^{3+}.[17,23] Evidently, the pristine Bi is almost entirely composed of Bi^0, but the BiO_x sample presents higher fractions of Bi existing in the Bi^{3+} state, again suggesting the partial oxidation of metallic Bi for the BiO_x sample.

The electrochemical properties of the Bi electrodes were evaluated in a three-electrode system with 1 M KOH as the aqueous electrolyte. The cyclic voltammetry (CV) curves of the pristine Bi and BiO_x electrodes show that two well-defined reduction peaks and oxidation peaks are distinctly identified with little distortion from 1 to 20 mV s^{-1} (Fig. S4†), confirming the good electrochemical behavior and highly reversible redox reaction of both electrodes. The two cathodic and anodic peaks may correspond to the two-step reaction in the KOH electrolyte described as the following: $Bi^0 - e^- \rightleftharpoons Bi^+$; $6Bi^+ + 6OH^- \rightleftharpoons Bi_2O_3 + 3H_2O + 4Bi^0$.[16] Encouragingly, the polarization between

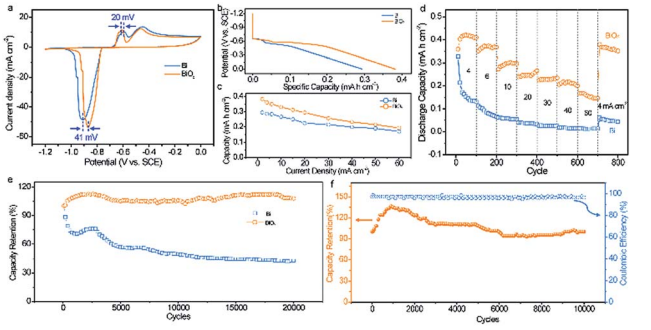

Fig. 2 (a) CV curves at 4 mV s^{-1}, (b) discharge curves at 2 mA cm^{-2}, (c) areal capacitance as a function of discharge current density, and (d) rate performance at various current densities of the Bi and BiO_x electrodes. (e) Cycling performance of the Bi and BiO_x electrodes for 20 000 cycles at 100 mV s^{-1}. (f) Cycling performance and coulombic efficiency of the BiO_x electrode at 40 mA cm^{-2}.

the oxidation and reduction peaks in the CV curve for the BiO_x electrode is visibly lower than that for the pristine Bi electrode (Fig. 2a), suggesting improved reversibility of the Bi electrode after surface oxidation. To gain insight into the difference in charge storage kinetics between the pristine Bi and BiO_x electrodes, log i (current density) *versus* log v (scan rate) of the anodic and cathodic peaks for both electrodes was plotted, and all emerge as nearly straight lines (Fig. S5†). Specifically, the b value determined from the slope of the cathodic peak for both electrodes is 0.51, meaning that the cathodic current is mostly controlled by semi-infinite diffusion. Meanwhile, the b values of the anodic peak for pristine Bi and BiO_x electrodes are 0.76 and 0.87, respectively, suggesting that the corresponding redox reactions at the peak regions of the BiO_x electrode are more affected by capacitive processes.

Fig. 2b compares the discharge profiles of the pristine Bi and BiO_x electrodes at a current density of 2 mA cm^{-2}. The BiO_x electrode delivers lower and longer discharge voltage plateaus than that of the pristine Bi electrode, implying its better electrochemical performance. At 2 mA cm^{-2}, a remarkable areal capacity of 0.38 mA h cm^{-2} is achieved by the BiO_x electrode, obviously higher than that of the pristine Bi electrode (0.29 mA h cm^{-2}) and other previously documented anodes for ARBs.[16,17,24] Of note, more than 50% capacity retention could still be maintained even at an ultrahigh current density of 60 mA cm^{-2} (Fig. 2c and S6†), which demonstrates its extraordinary rate capability. The rate performance of the BiO_x electrode is a little inferior to that of the pristine Bi owing to the increased charge transfer resistance (R_{ct}) after oxidation, which can be verified using the Nyquist plots (Fig. S7†). Within the current densities ranging from 2 to 60 mA cm^{-2}, the capacities of the BiO_x electrode are always higher than the values obtained for the pristine Bi electrode, indicating that the electrochemical properties of Bi are considerably boosted upon surface oxidation. The good rate property of the BiO_x electrode is further revealed in Fig. 2d, in which as the current density increases stepwise from 4 to 60 mA cm^{-2}, the discharge capacities are 0.358 and 0.167 mA h cm^{-2}, respectively. Meanwhile, as the current density switches back to 4 mA cm^{-2}, a significant capacity of 0.362 mA h cm^{-2} is retained after over 800 cycles at various current densities, revealing its excellent stability and reversibility of the redox reactions during an intense current fluctuation. In contrast, the pristine Bi displays a much poorer cycling performance than that of the BiO_x electrode. At a current density of 4 mA cm^{-2}, the pristine Bi presents an initial capacity of 0.327 mA h cm^{-2}, but decreases to only 0.045 mA h cm^{-2} after 800 cycles.

The unprecedented long-term durability is the most appealing property of the BiO_x electrode. As depicted in Fig. 2e, the capacity of the BiO_x electrode remains nearly unchanged even after 20 000 cycles, while only 42.6% capacity retention is maintained by the pristine Bi electrode. This value also outperforms the values of most recently reported anodes for ARBs or supercapacitors (SCs), such as Bi_2O_3 (74.5% after 200 cycles),[6] r-Bi_2O_3/GN (90% after 1000 cycles),[18] CNTs/Fe_2O_3 (96% after 1000 cycles),[24] VOS@C (92.3% after 10 000 cycles),[25] N–Fe_2O_3 (95.2% after 10 000 cycles),[26] and hierarchical Bi nanostructures (96% after 10 000 cycles).[16] SEM observations of the pristine Bi and BiO_x electrodes after cycling illustrated that both electrodes started to change after 5 cycles and underwent marked changes in morphology after 20 cycles derived from the repeated redox reaction between Bi and Bi^{3+} (Fig. S8 and S9†). Specifically, the pristine Bi underwent a larger morphology change for the first 50 cycles than the BiO_x sample, indicative of more structural damage for the pristine Bi for the first several cycles. Inductively coupled plasma emission spectroscopy (ICP) analysis gives more detailed evidence. As shown in Fig. S10,† the Bi concentration in the electrolyte after 20 000 cycles for the BiO_x electrode is lower than that of the pristine Bi electrode, confirming that the surface oxidation of the Bi electrode could mitigate the dissolution issue in the KOH electrolyte. Furthermore, the cycle life of the BiO_x electrode was further investigated at a high current density of 40 mA cm^{-2} (Fig. 2f). Significantly, the BiO_x electrode can maintain about 100% of its original capacity and over 95% coulombic efficiency after charging–discharging 10 000 cycles, manifesting again its excellent cycling property. In addition, the influence of the oxidation degree on the cycling stability of Bi was also studied. From XPS analysis, the ratio of O to Bi of pristine Bi increased sharply from 0.54 to 2.12 after surface oxidation for 25 cycles and then increased steadily to 2.15, 2.21, and 2.29 for 50, 100, and 200 cycles of oxidation (Fig. S11a†). Calculated by thermogravimetry results, the ratio of Bi_2O_3 to Bi is 0.21, 0.23, 0.27, and 0.33, respectively, for the BiO_x-25, BiO_x-50, BiO_x-100, and BiO_x-200 electrodes (Fig. S11b†). Above all, the oxidation degree increased gradually with the increment of ALD cycles. Indeed, surface oxidation of Bi could remarkably improve its cycle life to some extent and the Bi sample with 50 cycles of oxidation achieved the optimal performance (Fig. S12†). Besides, surface oxidation of the Bi electrode has little effect on its areal capacity (Fig. S13†).

To further elucidate the possible reasons for the enhanced cyclability of the BiO_x electrode, the chemical component changes of the Bi and BiO_x electrodes during the cycling process were monitored by *in situ* Raman spectroscopy. Fig. 3a displays the Raman spectra of the pristine Bi sample after certain cycles

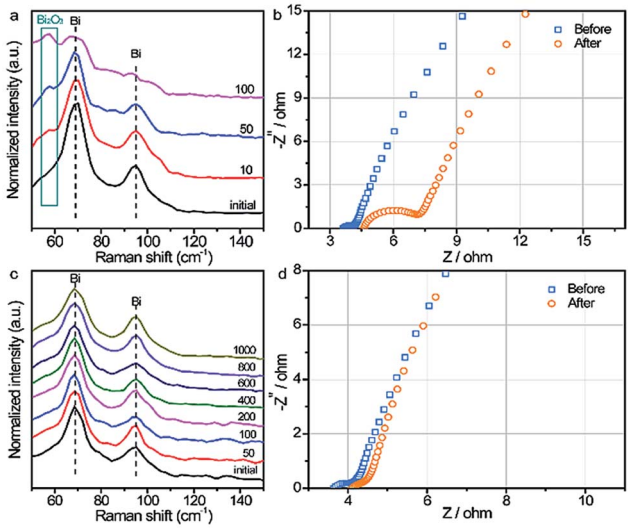

Fig. 3 (a) Raman spectra at different cycles and (b) Nyquist plots collected before and after cycling of the Bi electrode. (c) Raman spectra at different cycles and (d) Nyquist plots collected before and after cycling of the BiO_x electrode.

of the charging–discharging process. Obviously, the intensity of the characteristic Bi_2O_3 Raman peak (~55 cm^{-1}) emerges and increases gradually, while the peaks for metallic Bi weakening slightly after only 100 cycles, evidencing the formation of Bi_2O_3 derived from the irreversible reaction of pristine Bi during repeated cycling. By comparison, the Raman spectra for the BiO_x sample remain almost unchanged with two sharp metallic Bi peaks even after 1000 cycles (Fig. 3c), indicative of a highly reversible redox reaction of the BiO_x sample. Fig. S14† compares the Raman spectra of the pristine Bi and BiO_x electrodes after 20 000 cycles. The cycled pristine Bi electrode exhibits Raman peaks assigned to Bi_2O_3, which is absent for the cycled BiO_x electrode, implying again the irreversible oxidation of the pristine Bi during cycling.[22] Additionally, the ratios of O to Bi for the pristine Bi and BiO_x samples after certain cycles were evaluated by energy-dispersive spectroscopy (EDS) measurement (Table S1†). The ratios of O to Bi for the pristine Bi electrode increased gradually during the cycling process and reached 1.21 after 10 000 cycles, suggesting the formation of bismuth oxide during the charging–discharging process, in good agreement with the Raman spectroscopy result. In contrast, the ratios of O to Bi for the BiO_x electrode presented little increment even after 10 000 cycles, showing a reversible reaction for the BiO_x electrode. EIS was carried out to further elaborate the effect of the charging–discharging process on electronic properties. As observed in the Nyquist plots of the pristine Bi (Fig. 3b), the R_{ct} increased substantially after 20 000 cycles, which can explain the severe capacity decay of the pristine Bi. While for the BiO_x electrode, the R_{ct} values before and after 20 000 cycles are almost consistent (Fig. 3d), confirming its pronounced long-term stability during repetitive charging–discharging, in line with the Raman analysis. SEM images for the BiO_x electrode after ultrasound treatment for 1 h further verify that BiO_x NFs are adhered tightly and strongly to the carbon cloth substrate (Fig. S15†) Based on the above results, the remarkably boosted electrochemical performance of the BiO_x electrode is ascribed to the following reasons: (1) the OH^- adsorption ability of Bi could be improved after surface oxidation, further increasing its electrochemical performance; (2) the BiO_x electrode could effectively prevent the excessive oxidation of Bi during the charging–discharging process, contributing to enhanced reversibility; (3) the strategy of surface oxidation is able to mitigate the dissolution and capacity decay of the Bi electrode during the charging–discharging process; (4) the strong adhesive strength between the BiO_x NFs and carbon fiber surface means that the NFs will not easily fall off during the charging/discharging process. We further implemented this strategy by annealing the pristine Bi sample in air to assess its feasibility. As expected, the pristine Bi annealed at 200 °C for 5 min presented striking long-term cyclability with nearly no capacity decay after 20 000 cycles (Fig. S16†), which is consistent with the BiO_x electrode. In contrast, the Bi electrode annealed under a N_2 atmosphere at 200 °C for 5 min exhibited much inferior cycling stability with 58.2% capacity retention after 20 000 cycles. Therefore, this proposed surface oxidation strategy holds great promise to improve the cycling performance of Bi.

With high rate capability and outstanding lifespan, the BiO_x electrode shows great promise as an advanced anode for high-power and reliable ARBs. Thus, a nickel–bismuth battery consisting of the BiO_x anode and Ni–NiO cathode was constructed (denoted as Ni//Bi battery). The Ni–NiO cathode was prepared *via* electroplating Ni on carbon cloth and a subsequent oxidation process (details are given in the Experimental section and ESI†). SEM images showed that a rough Ni–NiO film was coated tightly on the surface of carbon cloth (Fig. S17a†). The XRD pattern in Fig. S17b† presented that all peaks indexed well with the metallic Ni (JCPDS #65-2845), which might be ascribed to the slightly low content of NiO. The electrochemical test revealed that the as-prepared Ni–NiO electrode is a promising cathode in the KOH electrolyte (Fig. S18†). Fig. S19a† comparatively depicts the CV curves of the Ni–NiO cathode and BiO_x anode at 50 mV s^{-1}, in which both electrodes present well-defined redox peaks. The CV profiles of the Ni//Bi battery at different operating potentials demonstrate a suitable voltage window of 1.6 V (Fig. S19b†). As shown in Fig. S19c,† the CV curves of the Ni//Bi battery show similar shapes even at a high scan rate of 100 mV s^{-1}, revealing its fast and reversible charge storage capability. Additionally, the representative galvanostatic discharge curves of the Ni//Bi battery at various current densities are displayed in Fig. 4a and all have noticeable discharge plateaus. More importantly, the Ni//Bi battery delivered a strikingly high capacity of 0.356 mA h cm^{-2} at a current density of 2 mA cm^{-2}, surpassing the most recently reported ARBs, such as the aqueous $NiCo_2O_4$//Bi battery (0.08 mA h cm^{-2} at 1 mA cm^{-2}),[16] Zn//Co_3O_4 battery (0.153 mA h cm^{-2} at 2.1 mA cm^{-2}),[31] Li ion battery (0.157 mA h cm^{-2} at 1 mA cm^{-2}),[32] and $H_2V_3O_8$//Zn battery (0.289 mA h cm^{-2} at 1.2 mA cm^{-2}).[33] Moreover, a superb rate capability has been realized using this Ni//Bi battery, with 62.3% capacity retention when the current density is raised to 60 mA cm^{-2} (Fig. 4b).

The rate performance of the Ni//Bi battery is further investigated at a series of current densities ranging from 4 to 60 mA

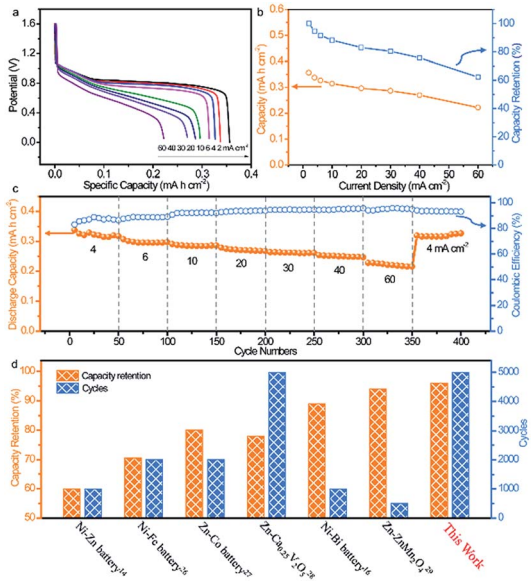

Fig. 4 (a) Discharge curves at various current densities, (b) areal capacity and capacity retention, (c) cycling performance and coulombic efficiency at various current density of the as-fabricated Ni//Bi battery. (d) Cycling performance comparison of the Ni//Bi battery with batteries reported in previous studies.[14,16,27–30]

cm^{-2} (Fig. 4c). The Ni//Bi battery exhibits discharge capacities of 0.338, 0.307, 0.29, 0.278, 0.263, 0.254, and 0.227 mA h cm^{-2} at 4, 6, 10, 20, 30, 40, and 60 mA cm^{-2}, respectively. When the current density was returned to 4 mA cm^{-2}, the discharge capacity recovered to 0.319 mA h cm^{-2} with a recovery ratio of 94.4%, suggesting that the Ni//Bi battery has fast reaction kinetics and excellent high rate performance. The prolonged cycling performance of the Ni//Bi battery at high rate (40 mA cm^{-2}) is illustrated in Fig. S20.† Encouragingly, an impressive capacity retention of 96% and a high coulombic efficiency approaching 100% were accomplished using the Ni//Bi battery over 5000 cycles, substantially outstripping most of the current ARBs (Fig. 4d, Table S1†).[14,16,27–30]

The energy density and power density of the Ni//Bi battery relative to existing ARBs and SCs were evaluated using Ragone plots. As plotted in Fig. 5a, our fabricated Ni//Bi battery delivered the highest volumetric energy density of 3.66 mW h cm^{-3}, which is considerably higher than that of the reported ARBs and SCs.[14,16,26,34,35] A remarkable volumetric power density of 0.436 W cm^{-3} was also achieved by the Ni//Bi battery, together with a high energy density of 1.61 mW h cm^{-3}, even much higher than most SCs.[37,39,41] With comparable energy density to commercial Li thin film batteries, our fabricated Ni//Bi battery generates ~4–80 times higher power density, suggesting its superfast charge–discharge ability.[27,42] To visually illustrate the potential of this Ni//Bi battery for practical applications, three prototype devices in series were employed to power a 3 V "Ni–Bi" shape light-emitting diode (LED) indicator and LED lights of a wristwatch effectively (Fig. 5b).

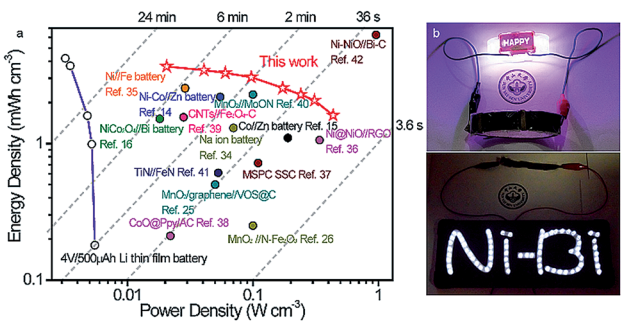

Fig. 5 (a) Ragone plots of the Ni//Bi battery, with the comparison of other recently developed energy storage devices.[14–16,25,26,34–42] (b) Pictures showing an LED indicator powered using the tandem Ni//Bi battery.

Conclusions

To summarize, a facile strategy of one-step surface oxidation was reported to significantly enhance the durability of Bi NFs. By improving the reaction reversibility, the optimized BiO_x electrode possessed outstanding cycle life with almost unattenuated capacity even after 20 000 cycles. Moreover, the BiO_x NF electrode with sufficient active sites delivered a remarkable areal capacity of 0.38 mA h cm^{-2} at 2 mA cm^{-2} as well as favorable rate capability (0.19 mA h cm^{-2} at 60 mA cm^{-2}). Capitalizing on the as-prepared BiO_x NF anode, we assembled a high performance aqueous Ni//Bi battery, affording excellent durability with 96% capacity retention after 5000 cycles. Furthermore, a maximum energy density of 3.66 mW h cm^{-3} was achieved by the Ni//Bi battery, together with a high power density of 0.436 W cm^{-3}, surpassing the most recently reported ARBs. This successive water oxidation strategy could provide a certain reference to the relevant materials.

Conflicts of interest

There are no conflicts to declare.

Acknowledgements

This work was financially supported by the National Natural Science Foundation of China (21822509, U1810110, 31530009 and 51672315), Guangdong Natural Science Funds for Distinguished Young Scholar (2014A030306048), Tip-top Scientific and Technical Innovative Youth Talents of Guangdong Special Support Program (2015TQ01C205), Pearl River Nova Program of Guangzhou (201610010080), the Science and Technology Planning Project of Guangzhou City for International Cooperation Program (20170430020). We also acknowledge the Photoemission Endstations (BL10B) in the National Synchrotron Radiation Laboratory (NSRL) for help in characterization.

Notes and references

1 F. Wan, L. Zhang, X. Dai, X. Wang, Z. Niu and J. Chen, *Nat. Commun.*, 2018, **9**, 1656.

2 J. Zhou, Z. Jiang, S. Niu, S. Zhu, J. Zhou, Y. Zhu, J. Liang, D. Han, K. Xu, L. Zhu, X. Liu, G. Wang and Y. Qian, *Chem*, 2018, **4**, 372–385.
3 Y. Zhong, X. Xia, S. Deng, J. Zhan, R. Fang, Y. Xia, X. Wang, Q. Zhang and J. Tu, *Adv. Energy Mater.*, 2018, **8**, 1701110.
4 L. Hu, C. Shi, K. Guo, T. Zhai, H. Li and Y. Wang, *Angew. Chem., Int. Ed.*, 2018, **57**, 8214–8218.
5 M. Song, H. Tan, D. Chao and H. J. Fan, *Adv. Funct. Mater.*, 2018, **28**, 1802564.
6 W. Zuo, W. Zhu, D. Zhao, Y. Sun, Y. Li, J. Liu and X. W. Lou, *Energy Environ. Sci.*, 2016, **9**, 2881–2891.
7 X. Wu, Y. Qi, J. J. Hong, Z. Li, A. S. Hernandez and X. Ji, *Angew. Chem., Int. Ed.*, 2017, **56**, 13026–13030.
8 F. Wang, O. Borodin, T. Gao, X. Fan, W. Sun, F. Han, A. Faraone, J. A. Dura, K. Xu and C. Wang, *Nat. Mater.*, 2018, **17**, 543–549.
9 J. Huang, Z. Wang, M. Hou, X. Dong, Y. Liu, Y. Wang and Y. Xia, *Nat. Commun.*, 2018, **9**, 2906.
10 J. F. Parker, C. N. Chervin, I. R. Pala, M. Machler, M. F. Burz, J. W. Long and D. R. Rolison, *Science*, 2017, **356**, 415–418.
11 M. Gong, Y. Li, H. Zhang, B. Zhang, W. Zhou, J. Feng, H. Wang, Y. Liang, Z. Fan, J. Liu and H. Dai, *Energy Environ. Sci.*, 2014, **7**, 2025–2032.
12 J. Liu, C. Guan, C. Zhou, Z. Fan, Q. Ke, G. Zhang, C. Liu and J. Wang, *Adv. Mater.*, 2016, **28**, 8732–8739.
13 Y. Zeng, Z. Lai, Y. Han, H. Zhang, S. Xie and X. Lu, *Adv. Mater.*, 2018, **30**, 1802396.
14 Y. Huang, W. S. Ip, Y. Y. Lau, J. Sun, J. Zeng, N. S. S. Yeung, W. S. Ng, H. Li, Z. Pei, Q. Xue, Y. Wang, J. Yu, H. Hu and C. Zhi, *ACS Nano*, 2017, **11**, 8953–8961.
15 M. Li, J. Meng, Q. Li, M. Huang, X. Liu, K. A. Owusu, Z. Liu and L. Mai, *Adv. Funct. Mater.*, 2018, **28**, 1802016.
16 Y. Zeng, Z. Lin, Y. Meng, Y. Wang, M. Yu, X. Lu and Y. Tong, *Adv. Mater.*, 2016, **28**, 9188–9195.
17 H. Xu, X. Hu, H. Yang, Y. Sun, C. Hu and Y. Huang, *Adv. Energy Mater.*, 2015, **5**, 1401882.
18 R. Liu, L. Ma, G. Niu, X. Li, E. Li, Y. Bai and G. Yuan, *Adv. Funct. Mater.*, 2017, **27**, 1701635.
19 W. Zuo, P. Xu, Y. Li and J. Liu, *Nanomaterials*, 2015, **5**, 1756–1765.
20 J. Sun, J. Wang, Z. Li, L. Niu, W. Hong and S. Yang, *J. Power Sources*, 2015, **274**, 1070–1075.
21 Q. Zhang, M. D. Levi, Q. Dou, Y. Lu, Y. Chai, S. Lei, H. Ji, B. Liu, X. Bu, P. Ma and X. Yan, *Adv. Energy Mater.*, 2019, **9**, 1802707.
22 K. Trentelman, *J. Raman Spectrosc.*, 2009, **40**, 585–589.
23 P. Zhang, Y. Zeng, M. Wang, W. Xu, Y. Liu and X. Lu, *J. Mater. Chem. A*, 2018, **6**, 8895–8900.
24 J. Liu, M. Chen, L. Zhang, J. Jiang, J. Yan, Y. Huang, J. Lin, H. J. Fan and Z. X. Shen, *Nano Lett.*, 2014, **14**, 7180–7187.
25 T. Zhai, X. Lu, Y. Ling, M. Yu, G. Wang, T. Liu, C. Liang, Y. Tong and Y. Li, *Adv. Mater.*, 2014, **26**, 5869–5875.
26 X. Lu, Y. Zeng, M. Yu, T. Zhai, C. Liang, S. Xie, M. S. Balogun and Y. Tong, *Adv. Mater.*, 2014, **26**, 3148–3155.
27 C. Guan, W. Zhao, Y. Hu, Q. Ke, X. Li, H. Zhang and J. Wang, *Adv. Energy Mater.*, 2016, **6**, 1601034.
28 X. Wang, F. Wang, L. Wang, M. Li, Y. Wang, B. Chen, Y. Zhu, L. Fu, L. Zha, L. Zhang, Y. Wu and W. Huang, *Adv. Mater.*, 2016, **28**, 4904–4911.
29 C. Xia, J. Guo, P. Li, X. Zhang and H. N. Alshareef, *Angew. Chem., Int. Ed.*, 2018, **57**, 3943–3948.
30 N. Zhang, F. Cheng, Y. Liu, Q. Zhao, K. Lei, C. Chen, X. Liu and J. Chen, *J. Am. Chem. Soc.*, 2016, **138**, 12894–12901.
31 L. Ma, S. Chen, H. Li, Z. Ruan, Z. Tang, Z. Liu, Z. Wang, Y. Huang, Z. Pei, J. A. Zapien and C. Zhi, *Energy Environ. Sci.*, 2018, **11**, 2521–2530.
32 X. Dong, L. Chen, J. Liu, H. Servane, Y. Wang and Y. Xia, *Sci. Adv.*, 2016, **2**, e1501038.
33 P. He, Y. Quan, X. Xu, M. Yan, W. Yang, Q. An, L. He and L. Mai, *Small*, 2017, **13**, 1702551.
34 S. Dong, L. Shen, H. Li, G. Pang, H. Dou and X. Zhang, *Adv. Funct. Mater.*, 2016, **26**, 3703–3710.
35 H. Wang, Y. Liang, M. Gong, Y. Li, W. Chang, T. Mefford, J. Zhou, J. Wang, T. Regier, F. Wei and H. Dai, *Nat. Commun.*, 2012, **3**, 917.
36 R. Li, Y. Wang, C. Zhou, C. Wang, X. Ba, Y. Li, X. Huang and J. Liu, *Adv. Funct. Mater.*, 2015, **25**, 5384–5394.
37 M. Yu, D. Lin, H. Feng, Y. Zeng, Y. Tong and X. Lu, *Angew. Chem., Int. Ed.*, 2017, **56**, 5454–5459.
38 M. Yu, X. Cheng, Y. Zeng, Z. Wang, Y. Tong, X. Lu and S. Yang, *Angew. Chem., Int. Ed.*, 2016, **55**, 6762–6766.
39 M. Yu, W. Wang, C. Li, T. Zhai, X. Lu and Y. Tong, *NPG Asia Mater.*, 2014, **6**, e129.
40 C. Zhu, P. Yang, D. Chao, X. Wang, X. Zhang, S. Chen, B. K. Tay, H. Huang, H. Zhang, W. Mai and H. J. Fan, *Adv. Mater.*, 2015, **27**, 4566–4571.
41 C. Zhou, Y. Zhang, Y. Li and J. Liu, *Nano Lett.*, 2013, **13**, 2078–2085.
42 Y. Zeng, Z. Lin, Z. Wang, M. Wu, Y. Tong and X. Lu, *Adv. Mater.*, 2018, **30**, 1707290.